Journal of Colloid and Interface Science 582 (2021) 283–290

Contents lists available at ScienceDirect

Journal of Colloid and Interface Science

journal homepage: www.elsevier.com/locate/jcis

Determination of contact angles for three-phase flow in porous media using an energy balance

Martin J. Blunt *, Abdulla Alhosani, Qingyang Lin, Alessio Scanziani, Branko Bijeljic

Department of Earth Science and Engineering, Imperial College London, London SW7 2BP, UK

GRAPHICAL ABSTRACT

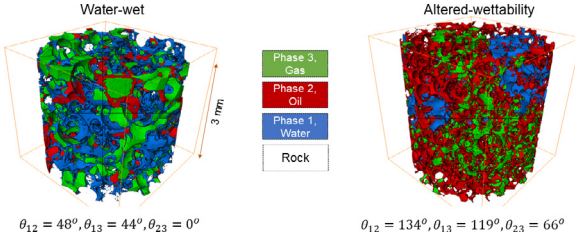

ARTICLE INFO

Article history:
Received 2 June 2020
Revised 30 July 2020
Accepted 31 July 2020
Available online 6 August 2020

Keywords:
Contact angle
Imaging
Wettability
Multiphase flow in porous media
Curvature
Three-phase flow

ABSTRACT

Hypothesis: We define contact angles, θ, during displacement of three fluid phases in a porous medium using energy balance, extending previous work on two-phase flow. We test if this theory can be applied to quantify the three contact angles and wettability order in pore-scale images of three-phase displacement.

Theory: For three phases labelled 1, 2 and 3, and solid, *s*, using conservation of energy ignoring viscous dissipation $(\Delta a_{1s}\cos\theta_{12} - \Delta a_{12} - \phi\kappa_{12}\Delta S_1)\sigma_{12} = (\Delta a_{3s}\cos\theta_{23} + \Delta a_{23} - \phi\kappa_{23}\Delta S_3)\sigma_{23} + \Delta a_{13}\sigma_{13}$, where ϕ is the porosity, σ is the interfacial tension, a is the specific interfacial area, S is the saturation, and κ is the fluid–fluid interfacial curvature. Δ represents the change during a displacement. The third contact angle, θ_{13} can be found using the Bartell-Osterhof relationship. The energy balance is also extended to an arbitrary number of phases.

Findings: X-ray imaging of porous media and the fluids within them, at pore-scale resolution, allows the difference terms in the energy balance equation to be measured. This enables wettability, the contact angles, to be determined for complex displacements, to characterize the behaviour, and for input into pore-scale models. Two synchrotron imaging datasets are used to illustrate the approach, comparing the flow of oil, water and gas in a water-wet and an altered-wettability limestone rock sample. We show that in the water-wet case, as expected, water (phase 1) is the most wetting phase, oil (phase 2) is intermediate wet, while gas (phase 3) is most non-wetting with effective contact angles of $\theta_{12} \approx 48^\circ$ and $\theta_{13} \approx 44^\circ$, while $\theta_{23} = 0$ since oil is always present in spreading layers. In contrast, for the altered-wettability case, oil is most wetting, gas is intermediate-wet, while water is most non-wetting with contact angles of $\theta_{12} = 134^\circ \pm \sim 10^\circ, \theta_{13} = 119^\circ \pm \sim 10^\circ$, and $\theta_{23} = 66^\circ \pm \sim 10^\circ$.

* Corresponding author.
E-mail address: m.blunt@imperial.ac.uk (M.J. Blunt).

https://doi.org/10.1016/j.jcis.2020.07.152
0021-9797/

1. Energy balance for three-phase flow

1.1. Introduction and the Young equation

We will determine fluid–fluid contact angles within a porous medium using energy balance. The derivation is based on previous work [1] where the contact angle is defined from a generalized Young equation [2,3]. The novelty here is to extend the treatment from two-phase [4] to three-phase flow and then to apply it to two dynamic experiments where pore-scale images of three-phase flow have been acquired [5,6]. The work has myriad applications to understand carbon dioxide storage [7], enhanced oil recovery [8], as well as food processing [9], drug delivery [10], and the design of micro-fluidics devices [11]. Multiphase flow is also seen in catalytic processes, such as the removal of non-aqueous phase pollutants from groundwater [12].

We generalize the theory for any number of fluid phases. We calculate the change in Helmholtz free energy: relating the work done from injecting the fluids to the change in surface energy ignoring viscous dissipation [1]. This approach is complementary to techniques that measure the so-called geometric contact angle on pore-space images directly [13–15], or estimates based on curvature and topology [16–18]: these methods are valuable to characterize wettability but do not directly find the contact angle associated with a displacement event, or the values needed in a numerical pore-scale model of multiphase flow.

We have three phases labelled 1, 2 and 3 and a solid s. We have three combinations of fluid pairs that can contact the surface: 12, 13 and 23, see Fig. 1. The contact angle θ_{12} measured through phase 1 in the presence of phase 2 is defined by the Young equation as:

$$\sigma_{12}\cos\theta_{12} = \sigma_{2s} - \sigma_{1s}, \tag{1}$$

where σ represents an interfacial tension or the energy per unit area of an interface. In Eq. (1) the contact angle is obtained from an energy balance and represents an effective value where the area is measured at a fixed resolution from an image [19]. Therefore the contact angle is not necessarily the angle that would be found at the atomic scale; it is, instead an effective value valid at the scale of the measurement.

Similar Young-type equations can be written for the other pairs of fluids:

$$\sigma_{13}\cos\theta_{13} = \sigma_{3s} - \sigma_{1s}, \tag{2}$$

$$\sigma_{23}\cos\theta_{23} = \sigma_{3s} - \sigma_{2s}. \tag{3}$$

It is possible to rearrange Eqs. (1)–(3) to obtain the Bartell-Osterhof relationship [21] assuming that the three phases are in mutual equilibrium, as illustrated in Fig. 1:

$$\sigma_{13}\cos\theta_{13} = \sigma_{12}\cos\theta_{12} + \sigma_{23}\cos\theta_{23}. \tag{4}$$

1.2. Calculation of the change in surface energy on displacement

Here we will calculate the change in surface energy during a displacement involving three fluid phases. The surface or interfacial energy of the fluids and solid in the pore space with areas, A, is:

$$E = A_{1s}\sigma_{1s} + A_{2s}\sigma_{2s} + A_{3s}\sigma_{3s} + A_{12}\sigma_{12} + A_{13}\sigma_{13} + A_{23}\sigma_{23}. \tag{5}$$

The total area of the solid surface $A_s = A_{1s} + A_{2s} + A_{3s}$ is constant.

We eliminate $A_{2s} = A_s - A_{1s} - A_{3s}$ and hence Eq. (5) becomes:

$$E = A_s\sigma_{2s} + A_{1s}(\sigma_{1s} - \sigma_{2s}) + A_{3s}(\sigma_{3s} - \sigma_{2s}) + A_{12}\sigma_{12} + A_{13}\sigma_{13} + A_{23}\sigma_{23}. \tag{6}$$

Then from Eqs. (1) and (3), Eq. (6) becomes:

$$E = A_s\sigma_{2s} + (A_{12} - A_{1s}\cos\theta_{12})\sigma_{12} + (A_{23} + A_{3s}\cos\theta_{23})\sigma_{23} + A_{13}\sigma_{13}. \tag{7}$$

We will now consider a change in energy during a displacement from one position of local equilibrium to another, as shown schematically in Fig. 2 for a series of capillary tubes.

Taking differences in Eq. (7) we find:

$$\Delta E = (\Delta A_{12} - \Delta A_{1s}\cos\theta_{12})\sigma_{12} + (\Delta A_{23} + \Delta A_{3s}\cos\theta_{23})\sigma_{23} + \Delta A_{13}\sigma_{13}. \tag{8}$$

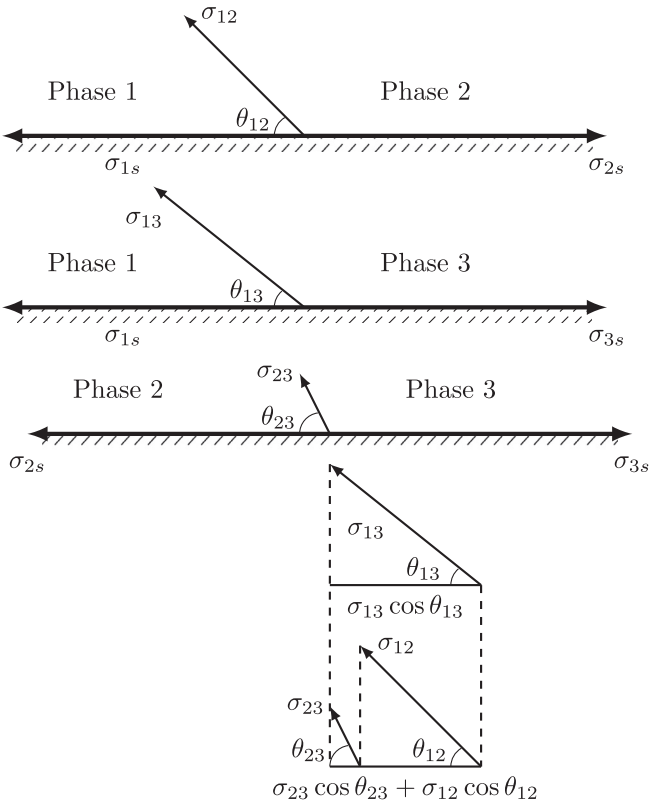

Fig. 1. Combinations of fluid phases in contact with a solid. For a three-phase system (phases 1, 2 and 3) there are three possible combinations, as shown from the top: 12, 13, and 23. The contact angles are measured through the denser phase and may assume any value between 0 and 180°: we normally associate phase 1 with water, phase 2 with oil, and phase 3 with gas. A horizontal force balance leads to the Young Eqs. (1)–(3) from which a relationship between the contact angles and fluid/fluid interfacial tensions may be derived, Eq. (4): this is illustrated geometrically in the bottom figure. Adapted from [20].

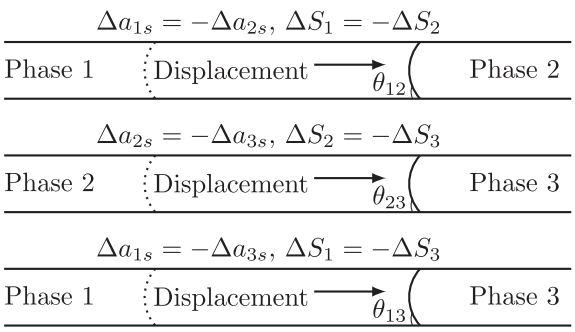

Fig. 2. A schematic of displacement in a bundle of capillary tubes. The contact angle, θ, is calculated using Eq. 17, based on an energy balance ignoring viscous dissipation. We treat the flow of three phases labelled 1, 2 and 3; s labels the solid. We find the changes in specific interfacial area, a and saturation, S.

At fixed temperature and volume the change in Helmholtz free energy will be zero [1,22,23]. The change in surface energy ΔE is equal to the work done to inject the fluids.

The capillary pressure is defined as $P_{cij} = P_j - P_i$ for any two phases i and j. In two-phase flow (with phases 1 and 2) the work done, $\Delta W = P_1\Delta V_1 + P_2\Delta V_2 = -P_{c12}\Delta V_1$ using $\Delta V_1 + \Delta V_2 = 0$ and $P_{c12} = P_2 - P_1$ [4]. Physically there is a negative sign since the work is positive if phase 1 increases its volume with a *higher* pressure than phase 2.

In three-phase flow, the calculation of work done can be extended by writing:

$$\Delta W = P_1\Delta V_1 + P_2\Delta V_2 + P_3\Delta V_3. \tag{9}$$

As with the consideration of surface energy, we can choose which volume to eliminate from the equation; to be consistent we take $\Delta V_2 = -\Delta V_1 - \Delta V_3$. Then

$$\Delta W = (P_1 - P_2)\Delta V_1 + (P_3 - P_2)\Delta V_3, \tag{10}$$

and using the definition of capillary pressure we find:

$$\Delta W = -P_{c12}\Delta V_1 + P_{c23}\Delta V_3. \tag{11}$$

Physically this can be thought of as displacement in two steps. First, that phase 1 displaces phase 2. The work done is, as in two-phase flow, $-P_{c12}\Delta V_1$. However phase 2 may displace phase 3, with a capillary pressure P_{c23}. The volume change is not simply ΔV_2 since some of this difference is due to the displacement of phase 2 by phase 1. Instead we consider the change in phase 3, and write the work done as $P_{c23}\Delta V_3$. Here the work done is positive if phase 2 has a higher pressure than phase 3, while ΔV_3 is negative. Whereas this equation was derived for the specific case of phase 1 that displaces 2, while phase 2 displaces phase 3, it is, in fact, correct for any injection sequence, evident from the form of Eq. (9).

To frame the analysis using conventional macroscopic quantities, we rewrite the work done in terms of saturation, $S : \Delta V_i = V\phi\Delta S_i$ for phase i. V is the total volume in which the energy balance is calculated while ϕ is the porosity. Then from Eq. (11):

$$\Delta W = V\phi(-P_{c12}\Delta S_1 + P_{c23}\Delta S_3). \tag{12}$$

The Young–Laplace equation will be used to relate the curvature κ_{ij} to the capillary pressure P_{cij} [24]:

$$P_{cij} = \sigma_{ij}\kappa_{ij}. \tag{13}$$

The signs are defined such that a positive curvature, with a positive capillary pressure P_{cij}, is when phase j bulges into phase i. Then Eq. (12) can be written:

$$\Delta W = V\phi(-\sigma_{12}\kappa_{12}\Delta S_1 + \sigma_{23}\kappa_{23}\Delta S_3). \tag{14}$$

Invoking conservation of energy: $\Delta E = \Delta W$ (an increase in surface energy is matched by a positive value of the work done), from Eqs. (8) and (14):

$$\begin{aligned}(\Delta A_{12} - \Delta A_{1s}\cos\theta_{12})\sigma_{12} + (\Delta A_{23} + \Delta A_{3s}\cos\theta_{23})\sigma_{23} + \Delta A_{13}\sigma_{13}\\ = V\phi(-\sigma_{12}\kappa_{12}\Delta S_1 + \sigma_{23}\kappa_{23}\Delta S_3).\end{aligned} \tag{15}$$

The specific surface area is defined as $a = A/V$, and then Eq. (15) becomes:

$$\begin{aligned}(\Delta a_{12} - \Delta a_{1s}\cos\theta_{12})\sigma_{12} + (\Delta a_{23} + \Delta a_{3s}\cos\theta_{23})\sigma_{23} + \Delta a_{13}\sigma_{13} =\\ \phi(-\sigma_{12}\kappa_{12}\Delta S_1 + \sigma_{23}\kappa_{23}\Delta S_3).\end{aligned} \tag{16}$$

Then rearranging:

$$\begin{aligned}&(\Delta a_{1s}\cos\theta_{12} - \Delta a_{12} - \phi\kappa_{12}\Delta S_1)\sigma_{12}\\ &= (\Delta a_{3s}\cos\theta_{23} + \Delta a_{23} - \phi\kappa_{23}\Delta S_3)\sigma_{23} + \Delta a_{13}\sigma_{13}.\end{aligned} \tag{17}$$

Eq. (17) is the main theoretical result of this paper. The important insight is that all the terms in Eq. (17), apart from the contact angles, can be determined from pore-space images (or indeed simulations) at two stages in a displacement. Interfacial areas [25], curvatures [26] and saturations can be measured on three-dimensional images. This analysis can be applied to pore-scale images of three-phase flow [27–29,5,30,31]. From this, the wettability of the system can be calculated: the contact angles θ represent the angles to be used in pore-scale models since they will correctly conserve energy for the displacement that has been observed. This removes the ambiguities associated with using geometrically-measured *in situ* angles [13], or angles measured on a flat surface.

When dealing directly with images, volumes are measured by counting voxels of each phase. Therefore it is more convenient to rewrite Eq. (17) directly in terms of the change in volume of each phase, rather than porosity and saturation. We define a specific volume of each phase $\nu_i = V_i/V = \phi S_i$ and write:

$$(\Delta a_{1s}\cos\theta_{12} - \Delta a_{12} - \kappa_{12}\Delta\nu_1)\sigma_{12} = (\Delta a_{3s}\cos\theta_{23} + \Delta a_{23} - \kappa_{23}\Delta\nu_3)\sigma_{23} + \Delta a_{13}\sigma_{13}. \tag{18}$$

1.3. Simplifications

Eq. (17) is one equation with two unknowns: $\cos\theta_{12}$ and $\cos\theta_{23}$. An unambiguous determination therefore requires three or more images, with two difference equations. However, even in cases where Eq. (17) is only known once, it is often possible to eliminate one contact angle, or to determine one from a two-phase displacement. For instance, if we now associate label 1 with water, 2 with oil, and 3 with gas, we can consider the following. Firstly, before gas injection, there will often be a two-phase displacement in the pore space (normally waterflooding): this could be used to determine $\cos\theta_{12}$ from Eq. (17) eliminating all terms involving phase 3 (gas) and rearranging:

$$\Delta a_{1s}\cos\theta_{12} = \phi\kappa_{12}\sigma_{12}\Delta S_1 + \Delta a_{12}, \tag{19}$$

which is the two-phase expression derived in [4]. Then, with Eq. (19) to find $\cos\theta_{12}, \cos\theta_{23}$ is found from Eq. (17). However, this procedure does assume that the contact angle for waterflooding between oil and water is also representative for three-phase flow.

Another possibility, if only three-phase displacement data are available, is to consider situations where one of the contact angles is known. For instance, in a spreading system, where oil forms layers separating gas and water, $\cos\theta_{23} = 1$ such that gas does not contact water directly: $a_{13} = 0$. Then Eq. (17) can be used to determine $\cos\theta_{12}$ directly using

$$\begin{aligned}&(\Delta a_{1s}\cos\theta_{12} - \Delta a_{12} - \phi\kappa_{12}\Delta S_1)\sigma_{12}\\ &= (\Delta a_{3s} + \Delta a_{23} - \phi\kappa_{23}\Delta S_3)\sigma_{23}.\end{aligned} \tag{20}$$

A third possibility is near-miscible gas injection, where the interfacial tension between gas and oil σ_{23} is small (of order 1 mN/m or less) and so can be ignored in Eq. (17). In this case, θ_{23} cannot be accurately determined, but θ_{12} can be calculated from:

$$(\Delta a_{1s}\cos\theta_{12} - \Delta a_{12} - \phi\kappa_{12}\Delta S_1)\sigma_{12} = \Delta a_{13}\sigma_{13}. \tag{21}$$

Once the two contact angles $\cos\theta_{12}$ and $\cos\theta_{23}$ are determined, the third, $\cos\theta_{13}$, is found from the Bartell-Osterhof relationship, Eq. (4).

1.4. Discussion and approximations

The contact angles can be determined wherever we see a displacement with changes in interfacial area and saturation with a fluid meniscus present. It can be calculated as an average for the

whole domain, or more locally, say for each pore, if the image quality is sufficient [32]. However, the analysis does require high-resolution images with little noise to obtain accurate results. The uncertainty in the calculations is quantified later when we present the results from experimentally-obtained images.

We have assumed reversible displacement processes which means that we ignore viscous dissipation. This can be included in the analysis, but introduces an additional unknown in the equation — namely the magnitude of this effect [32]. The viscous dissipation can be as low as 10 % of the total energy for displacements in bead packs [1], although it can be more significant for drainage processes and in more heterogeneous porous media [22]. However, our emphasis will be on imbibition where there is less dissipation [32], and altered-wettability systems where κ_{12} (the curvature between oil and water) is small. In these cases, viscous dissipation has little impact on the calculated contact angles, because the work done for displacement is very small: the contact angle is controlled by changes in surface areas at almost constant overall energy. Finally, we assume that there is little change in capillary pressure during the displacement: the κ used in Eq. (17) in the examples shown later will be the average of the values measured before and after the displacement. These approximations will be examined when we present the experimental results with an estimate of the likely errors in the calculation of contact angle.

2. Extension to any number of phases

Before testing our theory on imaging datasets, energy balance is extended to an arbitrary number of fluid phases. If we have n phases present, there are $n(n-1)/2$ interfacial tensions, contact angles and curvatures. However, the Young and Young–Laplace equations enable constraints between interfacial tensions and curvatures, and between the contact angles and interfacial tensions to be found, such that there are only $n-1$ independent curvatures and contact angles [33]. We can write two similar sets of constraints:

$$\sigma_{ik}\kappa_{ik} = \sigma_{ij}\kappa_{ij} + \sigma_{jk}\kappa_{jk}, \tag{22}$$

$$\sigma_{ik}\cos\theta_{ik} = \sigma_{ij}\cos\theta_{ij} + \sigma_{jk}\cos\theta_{jk}, \tag{23}$$

for any arbitrary phases i,j and k, with the additional identities and definitions:

$$\sum_{i=1}^{n}\Delta a_{is} = 0, \tag{24}$$

$$\sum_{i=1}^{n}\Delta S_i = 0, \tag{25}$$

and

$$\kappa_{ij} = -\kappa_{ji}, \tag{26}$$

$$\cos\theta_{ij} = -\cos\theta_{ji}. \tag{27}$$

Then we can derive the energy balance following the same approach as before. We have an arbitrary choice of which fluid-surface area and saturation to eliminate first in the equations: here we have decided to remove a_{2s} and ΔS_2 – refer to Eq. (17) – but the final expressions are independent of this choice when the relations Eqs. (22)–(27) are used.

Some low temperature reservoirs in which CO_2 is injected may hold four fluid phases: water, oil, a vapour phase which is mainly CO_2, a liquid phase containing lighter hydrocarbon components and significant amounts of CO_2, and an oil phase with some dissolved CO_2 [34]. With four phases, 1, 2, 3 and 4, the energy balance in Eq. (17) can be extended to:

$$\begin{aligned}(\Delta a_{1s}\cos\theta_{12} - \Delta a_{12} - \phi\kappa_{12}\Delta S_1)\sigma_{12} \\ = (\Delta a_{3s}\cos\theta_{23} + \Delta a_{23} - \phi\kappa_{23}\Delta S_3)\sigma_{23} \\ + (\Delta a_{4s}\cos\theta_{24} + \Delta a_{24} - \phi\kappa_{24}\Delta S_4)\sigma_{24} + \Delta a_{13}\sigma_{13} \\ + \Delta a_{14}\sigma_{14} + \Delta a_{34}\sigma_{34}.\end{aligned} \tag{28}$$

This is only one equation for a system with three independent contact angles: two angles need to be estimated through an analysis of two or three-phase displacements.

Finally, for completeness, the extension of Eq. (28) to any number n of liquid phases is:

$$\begin{aligned}(\Delta a_{1s}\cos\theta_{12} - \phi\kappa_{12}\Delta S_1)\sigma_{12} = \sum_{i=3}^{n}(\Delta a_{is}\cos\theta_{2i} - \phi\kappa_{2i}\Delta S_i)\sigma_{2i} \\ + \sum_{j=i+1}^{n}\sum_{i=1}^{n}\Delta a_{ij}\sigma_{ij}.\end{aligned} \tag{29}$$

3. Application to two imaging datasets

3.1. Experimental details

We will now illustrate the application of this analysis to two imaging datasets [5,6]. High-resolution time-resolved pore-scale images of displacement into samples of a carbonate rock were acquired at the Diamond Light Source in Oxfordshire, UK using the I13 beamline. Details of the experiments, image analysis and the rock samples used have been published previously [35,5,6]; here, we simply report results to enable the calculation of effective, thermodynamic, contact angles. The rock was a Ketton carbonate, an oolithic limestone composed principally of calcite [35]. We associate phase 1 with water (brine), phase 2 with oil, and phase 3 with gas (nitrogen).

For comparison, two experiments are considered. In the first, refined oil was injected into a water-saturated sample (completely saturated with brine), followed by brine injection and then injection of gas (nitrogen at high pressure). The final displacement – for which we will calculate contact angles – was re-injection of brine. The image size in three dimensions was $1000 \times 1000 \times 900$ voxels with a voxel size of 3.58 μm. The rock is naturally water-wet and so we anticipate that $\theta_{12} < 90^\circ$: we refer to this as the water-wet experiment. Oil was seen to spread in layers between water near the solid surface and gas in the centre of the pore space: there was negligible contact between gas and water, with a gas-oil contact angle, θ_{23} of zero.

Saturation is measured from the segmented image and is defined as the fraction of the pore space occupied by each phase. The interfaces between the fluids, and the fluid phases and the solid were extracted and smoothed as described in [5,6]. Interfacial area was measured on these smoothed surfaces. The curvature used is the average value across the entire sample. In this simple example, we will calculate the contact angles using Eq. (20) taking the difference in saturations and interfacial areas between the end of gas injection and the end of the subsequent brine re-injection to determine θ_{12}. The values of κ used will be the mean of the values measured at the end of gas injection and brine re-injection. In this dataset the image quality was insufficient to compute contact angles during the displacement, as we only recorded small changes in saturation and area between each image. For the second experiment, we will measure contact angle during the displacement and assess uncertainty.

In the second experiment, oil extracted from a reservoir in the Middle East was injected into a brine-saturated sample at high pressure and temperature and left for a month. The sample then

remained in a closed bottle of the same crude oil at high temperature for a further 3 months. In this case, some of the oil could adhere to the solid and alter its wettability [36]. This process, called ageing, attempts to reproduce the wettability conditions encountered deep underground in oil reservoirs [37]. Therefore, we expect the oil–water (brine) contact angle to be larger. Before the experiment, the crude oil was replaced by a refined oil. Then the same displacement sequence as in the water-wet case was adopted: waterflooding followed by gas (high-pressure nitrogen) injection followed by brine re-injection. We will refer to this as the altered-wettability experiment. The procedure for measuring saturation, interfacial areas and curvature was the same as for the water-wet case. The images comprised $1050 \times 1050 \times 1060$ voxels with a voxel size of 3.5 μm. This is a more complex example, where gas and water competed to occupy the largest pore spaces: there were direct gas–water contacts, while oil was present in wetting layers close to the solid surface. In this case the use of an energy balance approach is valuable to determine the contact angles and wettability order (which phase is most wetting, intermediate-wet and non-wetting) during gas injection.

The image quality in the altered-wettability experiment was sufficient to study differences between each image taken during the displacement. We consider a time sequence of 47 images and 46 differences. Two differences could not return sensible results, likely due to uncertaintites in segmentation and image quality, and so were ignored in the analysis. We apply two approaches to find the contact angles. Firstly, we take three consecutive images, with two differences. This leads to two equations, Eq. (17) with two unknowns θ_{23} and θ_{12} which can be solved directly. This provides 23 sets of values, as we apply this method to every pair of differences. In six cases the equations could not return physical values for contact angles ($|\cos\theta| > 1$) leaving a set of 17 contact angles. The second approach is to find single values of θ_{23} and θ_{12} that best fit Eq. (17) using a least squares approximation approach.

For illustrative purposes, Fig. 3 shows the pore-scale arrangement of oil, water and gas at the end of gas injection for the two experiments. Table 1 provides the saturations and interfacial areas used to calculate the contact angles for the water-wet experiment; for the altered-wettability case, we have, as mentioned before, 47 sets of values during gas injection which are listed in the Supplementary Material together with the differences and contact angles obtained.

Table 1
Data used to compute contact angles for the water-wet experiment from [5]; the more extensive dataset used for the altered-wettability experiment is presented in the Supplementary Material. The porosity, ϕ, of the resolvable pore space was 0.147. Phases 1, 2 and 3 are water (brine), oil and gas respectively. GI refers to the end of gas injection and WF to the end of second water (brine) injection. In both experiments $\sigma_{12} = 52.1$ mN/m, $\sigma_{13} = 63.7$ mN/m, and $\sigma_{23} = 11.2$ mN/m.

Property	GI	WF	Difference Δ/mean (for κ)
S_1	0.301	0.359	0.058
S_3	0.539	0.341	−0.197
a_{12} mm^{-1}	0.179	0.362	0.183
a_{23} mm^{-1}	0.181	0.306	0.125
a_{1s} mm^{-1}	4.062	4.472	0.411
a_{3s} mm^{-1}	1.714	0.775	−0.939
κ_{12} mm^{-1}	17.039	15.642	16.341
κ_{23} mm^{-1}	20.950	20.112	20.531

3.2. Results for the water-wet case

For the water-wet experiment, as mentioned above, $\theta_{23} = 0$ and we use Eq. (20) and the values in Table 1 to find $\theta_{12} = 48^\circ$. This is consistent with the geometrically-measured mean contact angle of $47.6^\circ \pm 4.6^\circ$ [5]. For this case, the analysis simply confirms the wettability and agrees with direct measurement. Furthermore, this contact angle is also similar to values from two-phase flow in a water-wet sandstone which — in a pore-scale model — provided an accurate prediction of relative permeability [4]. Using Eq. (4) we find $\theta_{13} = 44^\circ$: the medium is also water-wet in the presence of gas. However, for a porous medium of altered wettability, the three-phase contact lines where two fluids meet the surface are likely to be pinned until the hinging contact angles reach values sufficient to move across a more oil-wet surface [36]: in this case we may see a difference between the geometric and thermodynamic contact angles, and it is the thermodynamic value that more accurately represents the displacement. Furthermore, the wettability order may be change, in that gas may no longer be the most non-wetting phase.

3.3. Results for the altered-wettability experiment

For the altered-wettability experiment, using consecutive sequences of three images we obtained 17 sets of values for contact angles using Eq. (17), see Table S4 in the Supplementary Mate-

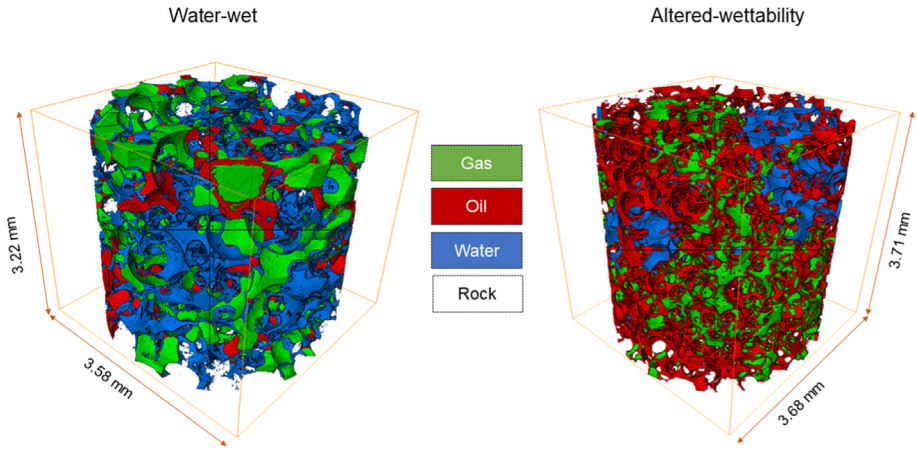

Fig. 3. Configurations of water (brine) in blue, oil in red and gas in green in the pore space after gas injection for the water-wet (left) and altered-wettability (right) experiments. The solid is transparent. The water-wet image analysed was $1000 \times 1000 \times 900$ voxels with a 3.58 μm voxel size. The altered-wettability image had $1050 \times 1050 \times 1060$ voxels with a 3.5 μm voxel size.

rial. Their mean and standard deviations were $\theta_{12} = 123^\circ \pm 19^\circ$ and $\theta_{23} = 59^\circ \pm 9^\circ$; using Eq. (4) we obtain $\theta_{13} = 110^\circ \pm 14^\circ$. There is a wide scatter in the data because we are looking at small differences between images. There is no discernable trend in contact angle during the displacement.

As mentioned in the previous section, another approach is to attempt to find a single average value representative for the whole sample during gas injection. The values of contact angle that best fit the data – that is, provided the most accurate match to Eq. (17) using a least-squares approach — was $\theta_{12} = 134^\circ$ and $\theta_{23} = 66^\circ$, and using Eq. (4) $\theta_{13} = 119^\circ$. Since this provides a consistent average value, we consider this a more reliable estimate than taking successive images separately.

This analysis shows that the rock is, on average, oil-wet whose oil–water contact angle is larger than 90°. θ_{12} was also calculated using Eq. (19) on the same sample from displacement of oil by water preceding gas injection: at the end of the displacement $\theta_{12} = 130^\circ \pm 5^\circ$ [38]. This is an important result, as there is an ambiguity in which contact angle to use in three-phase flow when gas displaces both water and oil in a system with altered wettability [39,40]: for this experiment the advancing contact angle (that is the value for water displacing oil, rather than a likely smaller receding angle for oil displacing water) best represents the displacement. The second observation is that in this system, when oil is more wetting, the gas-oil contact angle is not zero. While gas is still non-wetting to oil, gas contacts water directly — the oil does not everywhere spread between gas and water, as seen in the water-wet experiment. The final — and most significant — conclusion is that, on average, gas is more wetting than water: water is the most non-wetting phase, gas is intermediate-wet, while oil is most wetting, as predicted theoretically [41], and seen for three-phase flow at near-miscible conditions [42]. This implies that water will tend to occupy the larger pores and that the gas–water capillary pressure will be negative, as observed in the experiments [6]. The wetting state also affects the Gaussian curvature (the product of the principal curvatures in orthogonal directions): the average Gaussian curvatures of the interfaces between oil and water, and gas and oil, are negative during gas injection indicating well-connected phases [6]. For comparison, the geometric measurement of contact angle had an average value of $\theta_{23} = 57^\circ$, broadly consistent with our energy-balance results, but implied much less oil-wet conditions with $\theta_{12} = 105^\circ$ and $\theta_{13} = 81^\circ$ which suggests that water is still weakly wetting to gas [6]. This result is inconsistent with the displacement dynamics, and illustrates a limitation with the direct, geometric, measurement of contact angle that can record values on hinging contact lines which do not move during displacement. However, this analysis is based on a single, average measurement from one experiment: more work is required on several samples under different conditions to test how general these observations are.

3.4. Quantification of uncertainty

There are two principal sources of uncertainty in the analysis. The first concerns image quality and errors in the computation of interfacial areas and curvatures. This is evident in the high standard deviation in the results obtained from successive images. The principal uncertainty comes from the computation of curvature, where the radius of curvature of the interfaces is approximately 7 voxels. Previous work has shown that for this resolution the likely error in the calculation of curvature is up to 30 % [43]. Combining all segmentation and image analysis uncertainties, the error in the calculated average contact angle is approximately 7°.

The second, systematic, error is that we assume a reversible process and hence ignore viscous dissipation. In three-phase flow we encounter complex displacements with a combination of drainage and imbibition processes. In drainage as little as 36 % of the work is converted to surface energy [22]. This is potentially significant for the altered-wettability experiment where the rock is largely oil-wet, so both water and gas displacing oil are drainage. To quantify this effect we took the energy efficiency obtained in simulations for waterfooding a uniformly oil-wet rock with a contact angle of 135°: the viscous dissipation in this case was $R = 45$ % of the change in surface energy [32]. To compute contact angle including viscous dissipation we divide all the terms involving curvature (the work terms) in Eq. (17) by a factor $1 + R$ [32]. This leads to a decrease in the estimated value of θ_{12} of 10°. In our experiment, the amount of viscous dissipation is likely to be lower, as there is a range of contact angles, whose average value is below 135°. Furthermore, the displacement of water by gas is not a drainage process, so there is a mix of drainage, and imbibition for which the viscous dissipation is low with a negligible effect on the estimated contact angles [22,43].

Considering both viscous dissipation, and errors in our image segmentation and analysis, we estimate a likely uncertainty in the estimated contact angles of $\pm \sim 10^\circ$.

Overall, despite these sources of error, we have shown that the application of energy balance in three-phase flow can be used to quantify effective contact angles and to understand and interpret the displacement dynamics. These results could then be used as the basis for pore-scale modelling of three-phase flow.

4. Conclusions and implications

We have extended the concept of energy balance [1,4] to determine contact angles for three-phase flow. This approach provides the correct values to use in pore-scale models and avoids ambiguities associated with the direct measurement of a geometric contact angle, which does not necessarily capture a representative wettability during displacement [14].

We have illustrated the method by applying energy balance to two pore-scale imaging datasets for three-phase flow [5,6], quantifying the difference in wettability in a water-wet rock and another sample of the same rock type that had undergone a wettability alteration. We demonstrated that for the altered-wettability sample, in this case, oil was most wetting, gas was intermediate-wet and water was the most non-wetting phase, with an oil–water contact angle of approximately $\theta_{12} = 134^\circ$, a gas–water contact angle $\theta_{13} = 119^\circ$, and a gas-oil contact angle $\theta_{23} = 66^\circ$ The estimated uncertainty in the determination of contact angle is $\sim \pm 10^\circ$. This wettability order has been hypothesized previously [41], observed in micro-model studies [44], and inferred from the results of near-miscible gas injection experiments [42]. This result, however, conflicts with the assumptions used in traditional models of flow in oil reservoirs which assume that gas is the most non-wetting phase [20,45].

These contact angles can then be used as input into three-phase pore-scale models to accurately predict displacement processes, as well as the macroscopic properties relative permeability and capillary pressure [46,47].

Finally, we have showed how to extend the method to any number of fluid phases and provided general expressions for the relationships between interfacial tensions, contact angles and interfacial curvatures.

In future work we could apply this method to a variety of rock samples with images acquired using different techniques, as well as micro-model experiments. In addition, since contact angle may vary spatially, we could assess if the method could be performed locally, or even on a pore-by-pore basis to assess the variation in contact angle throughout a sample. This has been

attempted successfully in two-phase flow using simulation datasets [32], but not applied to experimental images. Lastly, we could apply this technique on benchmark images and simulations to quantify the sources of uncertainty and error in the estimates of contact angle.

Declaration of Competing Interest

The authors declare that they have no known competing financial interests or personal relationships that could have appeared to influence the work reported in this paper.

Acknowledgments

We are grateful to Abu Dhabi National Oil Company (ADNOC) for financial support. The data from the altered-wettability dataset can be obtained from the Digital Rocks Portal, www.digitalrocksportal.org/projects/253.

Appendix A. Supplementary material

Supplementary data associated with this article can be found, in the online version, at https://doi.org/10.1016/j.jcis.2020.07.152.

References

[1] N.R. Morrow, Physics and thermodynamics of capillary action in porous media, Industr. Eng. Chem. 62 (6) (1970) 32–56, https://doi.org/10.1021/ie50726a006.
[2] T. Young, An essay on the cohesion of fluids, Philos. Trans. R. Soc. Lond. 95 (1805) 65–87. http://www.jstor.org/stable/107159.
[3] N.K. Adam, Use of the term Young equation for contact angles, Nature 180 (1957) 809–810.
[4] M.J. Blunt, Q. Lin, T. Akai, B. Bijeljic, A thermodynamically consistent characterization of wettability in porous media using high-resolution imaging, J. Colloid Interface Sci. 552 (2019) 59–65, https://doi.org/10.1016/j.jcis.2019.05.026. http://www.sciencedirect.com/science/article/pii/S0021979719305648.
[5] A. Scanziani, K. Singh, H. Menke, B. Bijeljic, M.J. Blunt, Dynamics of enhanced gas trapping applied to CO2 storage in the presence of oil using synchrotron x-ray micro tomography, Appl. Energy 259 (2020) 114136.
[6] A. Scanziani, A. Alhosani, Q. Lin, C. Spurin, G. Garfi, M.J. Blunt, B. Bijeljic, In situ characterisation of three-phase flow in mixed-wet porous media using synchrotron imaging, Water Resour. Res. (2020) https://doi.org/10.1029/2020WR027873..
[7] V. Scott, R.S. Haszeldine, S.F.B. Tett, A. Oschlies, Fossil fuels in a trillion tonne world, Nat. Clim. Change (2015) 419–423, https://doi.org/10.1038/nclimate2578.
[8] L.W. Lake, Enhanced Oil Recovery, Prentice Hall Inc., Englewood Cliffs, New Jersey, 1989.
[9] R.N. Zúñiga, J.M. Aguilera, Aerated food gels: fabrication and potential applications, Trends Food Sci. Technol. 19 (2008) 176–187.
[10] K.W. Ferrara, M.A. Borden, H. Zhang, Lipid-shelled vehicles: Engineering for ultrasound molecular imaging and drug delivery, Acc. Chem. Res. 47 (2009) 881–892.
[11] Z. Chen, J. Xu, Y. Wang, Gas-liquid-liquid multiphase flow in microfluidic systems – a review, Chem. Eng. Sci. 202 (2019) 1–14.
[12] C. Descorme, Catalytic wastewater treatment: Oxidation and reduction processes. recent studies on chlorophenols, Catal. Today 297 (2017) 324–334, https://doi.org/10.1016/j.cattod.2017.03.039.
[13] M.G. Andrew, B. Bijeljic, M.J. Blunt, Pore-scale contact angle measurements at reservoir conditions using x-ray microtomography, Adv. Water Resour. 68 (2014) 24–31, https://doi.org/10.1016/j.advwatres.2014.02.014. http://www.sciencedirect.com/science/article/pii/S0309170814000372.
[14] A. Alratrout, A. Raeini, B. Bijeljic, M.J. Blunt, Automatic measurement of contact angle in pore-space images, Adv. Water Resour. 109 (2017) 158–169.
[15] K.A. Klise, D. Moriarty, H. Yoon, Z. Karpyn, Automated contact angle estimation for three-dimensional x-ray microtomography data, Adv. Water Resour. 95 (2016) 152–160, https://doi.org/10.1016/j.advwatres.2015.11.006. http://www.sciencedirect.com/science/article/pii/S0309170815002651.
[16] C. Sun, E. McClure, J, P. Mostaghimi, A.L. Herring, S. Berg, T. Armstrong, R, Probing effective wetting in subsurface systems, Geophysical Research Letters 47 (5) (2020) e2019GL086151, e2019GL086151 10.1029/2019GL086151. arXiv:https://agupubs.onlinelibrary.wiley.com/doi/pdf/10.1029/2019GL086151, doi:10.1029/2019GL086151. https://agupubs.onlinelibrary.wiley.com/doi/abs/10.1029/2019GL086151..
[17] C. Sun, J.E. McClure, P. Mostaghimi, H.A.L., M. Shabaninejad, S. Berg, R.T. Armstrong, Linking continuum-scale state of wetting to pore-scale contact angles in porous media, J. Colloid Interface Sci. 561 (2020) 173–180. doi: https://doi.org/10.1016/j.jcis.2019.11.105. URL http://www.sciencedirect.com/science/article/pii/S002197971931433X.
[18] M.J. Blunt, T. Akai, B. Bijeljic, Evaluation of methods using topology and integral geometry to assess wettability, J. Colloid Interface Sci. 576 (2020) 99–108.
[19] M.L. Brusseau, S. Peng, G. Schnaar, A. Murao, Measuring air-water interfacial areas with X-ray microtomography and interfacial partitioning tracer tests, Environ. Sci. Technol. 41 (6) (2007) 1956–1961. arXiv:https://doi.org/10.1021/es061474m, doi:10.1021/es061474m. doi: 10.1021/es061474m..
[20] M.J. Blunt, Multiphase Flow in Permeable Media: a Pore-Scale Perspective, Cambridge University Press, 2017.
[21] F.E. Bartell, H.J. Osterhof, Determination of the wettability of a solid by a liquid, Ind. Eng. Chem. 19 (1927) 1277–1280.
[22] S. Seth, N.R. Morrow, Efficiency of the conversion of work of drainage to surface energy for sandstone and carbonate, SPE Reserv. Eval. Eng. 10 (2007) 338–347, https://doi.org/10.2118/102490-PA.
[23] S. Berg, H. Ott, S.A. Klapp, A. Schwing, R. Neiteler, N. Brussee, A. Makurat, L. Leu, F. Enzmann, J.O. Schwarz, M. Kersten, S. Irvine, M. Stampanoni, Real-time 3D imaging of Haines jumps in porous media flow, Proc. Nat. Acad. Sci. 110 (10) (2013) 3755–3759. arXiv:http://www.pnas.org/content/110/10/3755.full.pdf, 10.1073/pnas.1221373110.
[24] P.S. Laplace, Traite de mecanique celeste (gauthier-villars, paris, 1839), suppl. au livre x, 1805 and 1806, resp, Oeuvres compl 4..
[25] K.A. Culligan, D. Wildenschild, B.S.B. Christensen, W.G. Gray, M.L. Rivers, A.F.B. Tompson, Interfacial area measurements for unsaturated flow through a porous medium, Water Resour. Res. 40 (12) (2004) W12413, https://doi.org/10.1029/2004WR003278.
[26] R.T. Armstrong, M.L. Porter, D. Wildenschild, Linking pore-scale interfacial curvature to column-scale capillary pressure, Adv. Water Resour. 46 (2012) 55–62, https://doi.org/10.1016/j.advwatres.2012.05.009. http://www.sciencedirect.com/science/article/pii/S0309170812001443.
[27] M. Feali, W. Pinczewski, Y. Cinar, C.H. Arns, J.Y. Arns, N. Francois, M.L. Turner, T. Senden, M.A. Knackstedt, Qualitative and quantitative analyses of the three-phase distribution of oil, water, and gas in bentheimer sandstone by use of micro-ct imaging, SPE Reserv. Eval. Eng. 15 (6) (2012) 706–711, https://doi.org/10.2118/151609-PA.
[28] M. Khishvand, A. Alizadeh, M. Piri, In-situ characterization of wettability and pore-scale displacements during two- and three-phase flow in natural porous media, Adv. Water Resour. 97 (2016) 279–298, https://doi.org/10.1016/j.advwatres.2016.10.009.
[29] A. Scanziani, K. Singh, T. Bultreys, B. Bijeljic, M.J. Blunt, In situ characterization of immiscible three-phase flow at the pore scale for a water-wet carbonate rock, Adv. Water Resour. 121 (2018) 446–455.
[30] A. Alhosani, A. Scanziani, Q. Lin, Z. Pan, B. Bijeljic, M.J. Blunt, In situ pore-scale analysis of oil recovery during three-phase near-miscible CO_2 injection in a water-wet carbonate rock, Adv. Water Resour. 134 (2019) 103432.
[31] Z. Qin, M. Arshadi, M. Piri, Micro-scale experimental investigations of multiphase flow in oil-wet carbonates. ii. tertiary gas injection and wag, Fuel 257 (2019) 116012, https://doi.org/10.1016/j.fuel.2019.116012.
[32] T. Akai, Q. Lin, B. Bijeljic, M.J. Blunt, Using energy balance to determine pore-scale wettability, J. Colloid Interface Sci. 576 (2020) 486–495, https://doi.org/10.1016/j.jcis.2020.03.074.
[33] M.J. Blunt, Constraints on contact angles for multiple phases in thermodynamic equilibrium, J. Colloid Interface Sci. 239 (1) (2001) 281–282, https://doi.org/10.1006/jcis.2001.7534. http://www.sciencedirect.com/science/article/pii/S0021979701975344.
[34] F.M. Orr, A.D. Yu, C.L. Lien, Phase behavior of CO2 and crude oil in low-temperature reservoirs, J. Petrol. Technol. 21 (1981) 480–485.
[35] M.G. Andrew, B. Bijeljic, M.J. Blunt, Pore-scale imaging of trapped supercritical carbon dioxide in sandstones and carbonates, Int. J. Greenhouse Gas Control 22 (2014) 1–14, https://doi.org/10.1016/j.ijggc.2013.12.018. http://www.sciencedirect.com/science/article/pii/S1750583613004519.
[36] A.R. Kovscek, H. Wong, C.J. Radke, A pore-level scenario for the development of mixed wettability in oil reservoirs, AIChE J. 39 (6) (1993) 1072–1085, https://doi.org/10.1002/aic.690390616.
[37] J.S. Buckley, Y. Liu, Some mechanisms of crude oil/brine/solid interactions, J. Petrol. Sci. Eng. 20 (3–4) (1998) 155–160, https://doi.org/10.1016/S0920-4105(98)00015-1. http://www.sciencedirect.com/science/article/pii/S0920410598000151.
[38] A. Scanziani, Q. Lin, A. Alhosani, M.J. Blunt, B. Bijeljic, Dynamics of displacement in mixed-wet porous media, Proceedings of the Royal Society A. 476 (2020) 20200040. http://dx.doi.org/10.1098/rspa.2020.0040..
[39] M. Piri, M.J. Blunt, Three-dimensional mixed-wet random pore-scale network modeling of two- and three-phase flow in porous media. i. model description, Phys. Rev. E 71 (2) (2005) 026301, https://doi.org/10.1103/PhysRevE.71.026301.
[40] M.I.J. van Dijke, K.S. Sorbie, Pore-scale network model for three-phase flow in mixed-wet porous media, Phys. Rev. E 66 (4) (2002) 046302, https://doi.org/10.1103/PhysRevE.66.046302. http://link.aps.org/doi/10.1103/PhysRevE.66.046302.
[41] M.I.J. van Dijke, K.S. Sorbie, An analysis of three-phase pore occupancies and relative permeabilities in porous media with variable wettability, Transp. Porous Media 48 (2) (2002) 159–185, https://doi.org/10.1023/A%3A1015692630733.

[42] A. Alhosani, A. Scanziani, Q. Lin, A.Q. Raeini, B. Bijeljic, M.J. Blunt, Pore-scale mechanisms of CO_2 storage in oilfields, Scient. Rep. 10 (2020) 8534, https://doi.org/10.1038/s41598-020-65416-z.
[43] T. Akai, Q. Lin, A. Alhosani, B. Bijeljic, M.J. Blunt, Quantification of uncertainty and best practice in computing interfacial curvature from complex pore space images, Materials 12 (2019) 2138, https://doi.org/10.3390/ma12132138.
[44] M.I.J. van Dijke, K.S. Sorbie, M. Sohrabi, A. Danesh, Simulation of wag floods in an oil-wet micromodel using a 2-d pore-scale network model, J. Petrol. Sci. Eng. 52 (1–4) (2006) 71–86, https://doi.org/10.1016/j.petrol.2006.03.014. http://www.sciencedirect.com/science/article/pii/S092041050600060X.
[45] H.L. Stone, Probability model for estimating three-phase relative permeability, J. Petrol. Technol. 22 (2) (1970) 214–218, https://doi.org/10.2118/2116-PA.
[46] M. Piri, M.J. Blunt, Three-dimensional mixed-wet random pore-scale network modeling of two- and three-phase flow in porous media. ii. results, Phys. Rev. E 71 (2) (2005) 026302, https://doi.org/10.1103/PhysRevE.71.026302.
[47] A.V. Ryazanov, M.I.J. van Dijke, K.S. Sorbie, Two-phase pore-network modelling: Existence of oil layers during water invasion, Transp. Porous Media 80 (1) (2009) 79–99, https://doi.org/10.1007/s11242-009-9345-x.